



Antiperovskite materials as promising candidates for efficient tandem photovoltaics: First-principles investigation

P.D. Sreedevi^{a,b}, R. Vidya^c, P. Ravindran^{a,b,*}

^a Department of Physics, Central University of Tamil Nadu, Thiruvavur, Tamil Nadu, 610005, India

^b Simulation Center for Atomic and Nanoscale MATerials (SCANMAT), Central University of Tamil Nadu, Thiruvavur, Tamil Nadu, 610005, India

^c Department of Medical Physics, Anna University, Chennai, Tamil Nadu, 600025, India

ARTICLE INFO

Keywords:

Antiperovskite materials
Structural features
Electronic and optical properties
Tandem photovoltaic applications
First principles calculation

ABSTRACT

In the past few years, the perovskite tandem solar cells show commendable developments in achieving the power conversion efficiency of 30% which is relatively higher than that produced by the single-junction solar cells. But, to the best of our knowledge, there is no literature available regarding the antiperovskite based tandem solar cells. This is the first study reporting the applicability of some predicted antiperovskite compounds Mg_3PN , Ca_3PN , Sr_3PN , Ba_3PN , $BaSr_2PN$, $Ba_{1.5}Sr_{1.5}PN$, and Ba_2SrPN with suitable properties for using as the best absorbing layers in higher efficient tandem solar cell. These seven antiperovskite compounds attain direct band gap nature with band gap values ranging from 1.1 eV to 2.3 eV. The absorption coefficient, optical conductivity and extinction coefficients are found relatively higher in the visible region. Besides, low reflectivity is also analysed in the visible region for the compounds. Low charge carrier effective masses and low recombination rate between the charge carriers can also be observed in the seven materials and thus boost up the carrier mobility and electrical conductivity. Besides, the excitonic binding energy values are also found to be very small for all the predicted compounds. Since all the compounds stabilize in the same crystal structure, the lattice mismatch between each cell will become so less which in turn will be beneficial for making the tandem solar cell. So, it is more suitable to use these materials as the absorbing layers in tandem solar cells apart from use them in single junction photovoltaics since the power conversion efficiency will be more for multijunction/tandem solar cells.

1. Introduction

Perovskite lead halides have emerged as a new class of materials with the spectacular properties suitable for using them as the best solar absorbers [1]. Owing to the excellent optoelectronic properties of hybrid perovskites (HPs), the certified power conversion efficiency (PCE) of perovskite based solar cells has increased up to 25.2%. The development is visible only in the last few years. It has been reported that the most applicable approach to transcend the Shockley–Queisser [2] limit of single-junction solar cells is the stacking of the narrow-bandgap and wide bandgap sub cells on top of the other which are usually called as tandem solar cells (TSCs) [3]. These multijunction solar cells or TSCs allow higher efficiencies than single-junction solar cells by efficiently utilising the energy of short-wavelength photons in the spectrum of sunlight. It has been proved that these ABX_3 perovskite materials are the most suitable candidates for using them as the absorbing layer in TSCs. Comparing with the remarkable achievement of using many

perovskites-based materials as the absorbing layer in TSCs, the perovskite-counterparts, *i.e.* the antiperovskite based tandem solar cells has not yet been adequately identified and reported. Since they adopt an A_3BX structure (inverse of ABX_3 perovskite structure, where A , B are cations and X is the anion), there is a great possibility for the antiperovskites [4] materials to use them as efficient absorbing layers for TSCs.

The prime novelty of the present work is the prediction and design of some more antiperovskite materials with suitable properties that can be used as the absorbing layers in TSCs. For that, the antiperovskites incorporating Group II-A (alkaline-earth (AE)) elements [5] are much preferred to use due to the diverse applications of these in electronics, mechanics, and military [6].

The crystal structures of many Group-2A based antiperovskites have resolved and many properties for such compounds have also been studied by experimentally and theoretically by several research groups [5,7–32].

* Corresponding author. Department of Physics, Central University of Tamil Nadu, Thiruvavur, Tamil Nadu, 610005, India.

E-mail address: raviphy@cutn.ac.in (P. Ravindran).

<https://doi.org/10.1016/j.mssp.2022.106727>

Received 6 February 2022; Received in revised form 2 April 2022; Accepted 12 April 2022

Available online 25 April 2022

1369-8001/© 2022 Elsevier Ltd. All rights reserved.

The accumulative research survey gives direct evidence that an accurate structural optimization using a large number of similar available compounds and detailed analysis of the structural information for Mg_3PN , Ca_3PN , Sr_3PN , Ba_3PN need to be done for understanding the potential features of the compounds. Herein, we have reported the ground-state crystal structures of five ternary antiperovskite compounds A_3PN , ($A = Mg, Ca, Sr, Ba, \text{ and } Zn$) that are found out from the density functional theory (DFT) prediction method by considering 32 potential structural variants as the representative prototypes. As we intend to select non-toxic and earth-abundant elements to design solar cell materials, we have excluded the toxic elements Be, Ra from the AE group and selected the divalent transition element Zn. This is the first ever study based on the structural and electronic properties compound Zn_3PN . So, here, we project a detailed analysis on the structural, electronic, and optical properties of the predicted compounds in their predicted crystal structure. Apart from these studies, the tailoring of the band gap has been done to check whether we can have more materials with direct band gap behaviour and near-optimum band gap value with enhanced optical absorption to use them as the absorber layers in higher efficiency TSCs. For applying the predicted compounds for practical usage, further experimental studies and experimental confirmations are required.

2. Structure prediction methodology and computational details

We have employed density functional theory-based computations to determine the total energy of these compounds. The thirty two potential structure types as inputs in the structural optimization calculations for the A_3PN compounds are: $CaCO_3(Ama2)$; $BaTiO_3(Amm2)$; $ZnSiO_3(C12C1)$; $PbZrO_3(Cm2\ m)$; $CaSnO_3(Fm-3c)$; $KSbO_3(Fd3m)$; $SrZrO_3(I4/mcm)$; $CdGeO_3(B11b)$; $NaNbO_3(P2_1ma)$; $SrZrO_3(Bmnb)$; $BaPbO_3(I12/m1)$; $BaPbO_3(Ibmm)$; $LaMnO_3(P121/a)$; $PbSeO_3(P121/m1)$; $NaClO_3(P123)$; $BaSiO_3(P212121)$; $NaTaO_3(P4/mbm)$; $BaTiO_3(P4/mmm)$; $LiIO_3(P63)$; $BaNiO_3(P63/mmc)$; $CuGeO_3(Pbmm)$; $YFeO_3(Pbn21)$; $LaTiO_3(Pbnn)$; $CaZrO_3(Pcmm)$; $SrTiO_3(Pm\bar{3}m)$; $NaNbO_3(Pmmm)$; $GdVO_3(Pmnb)$; $MgSeO_3(Pnma)$; $BiFeO_3(R3c)$; $LaCuO_3(R-3c)$; $BaTbO_3(R-3cR)$; and $BaRuO_3(R-3m)$. From the lowest total energy configuration of these considered 32 structural variants, we have identified the ground state structure of these compounds.

The total energy calculations for all these compounds in the above mentioned 32 structural variants were executed with projector-augmented-wave (PAW) [33] method as implemented in the Vienna *ab initio* simulation package (VASP) [34]. The exchange-correlation effects are treated by generalized gradient approximation (GGA) [35] of Perdew, Burke, and Ernzerhof (PBE). The structural optimization in the considered 32 structures was done by converging the stress and force into a relaxed state. The total energies were calculated using plane wave with cut-off energy of 520 eV and Monkhorst-Pack Brillouin zone method [36] with sufficient k-point density. We have treated the Mg ($3s^2$), Ca ($3s^2-3p^6-4s^2$), Sr ($4s^2-4p^6-5s^2$), Ba ($5s^2-5p^6-6s^2$) and Zn ($3d^{10}-4s^2$) as valence electrons in the PAW potentials. The tolerance for the total energy convergence was set to 1×10^{-6} eV atom⁻¹ and the maximum ionic Hellmann-Feynman force was set within 0.01eV \AA^{-1} for the ionic relaxation. The input computational parameters are chosen in such a way to obtain well converged total energy and the resultant properties. The energy vs volume (E-V) graphs are plotted for various structures in each compound to find the energetically lowest structural configurations. This E-V curve was further fitted to the Murnaghan equation of states [37] to obtain the equilibrium volume and bulk modulus.

The electronic properties were calculated for the compounds in their corresponding predicted ground state crystal-structures. For the electronic properties, we used Heyd-Scuseria-Ernzerhof (HSE06) [38] based hybrid functional to manage exchange-correlation for achieving the accurate band structure and energy band gap values. The nature of the chemical bonding between the constituent elements in the compounds is

analysed from the density of states plots (TDOS, PDOS) [39]. More information on the chemical bonding behaviour was gained from the charge density analysis [40]. Some of the linear optical properties which show more relevance for photovoltaic applications [41–45] are calculated with denser k-point mesh by sampling in the irreducible Brillouin zone and plotted in this paper. The origin of each bands and the absorption peaks are further analysed using p4Vasp [46], which is the VASP visualization tool.

We could successfully deliberate the charge carrier effective mass calculation using VASPKIT [47]. We used higher number of k-points in the effective mass calculation for obtaining accurate electron and the hole effective mass values.

3. Results and analysis

3.1. Crystal structures of A_3PN series

The structural optimization technique using different prototypes will be accurate and reliable only when we consider a greater number of structural variants as input into the structural optimization calculation. In order to get the correct ground state crystal structure for the considered compounds, we have selected 32 space groups with different symmetry. Among the considered 32 structure types, we found that the most stable crystal structure for all these five A_3PN ($A = Mg, Ca, Sr, Ba$ and Zn) compounds are in orthorhombic symmetry with space group $P2_1ma$ (space group no, 26; $NaNbO_3$ structure type). We have illustrated the E-V curves for Ca_3PN with potential lower energy configurations in Fig. 1. From this figure it is apparent that among the lower energy structural variants, Ca_3PN possess $P2_1ma$ ($NaNbO_3$) structure type as its ground state structure. Likewise, we were able to get $P2_1ma$ ($NaNbO_3$) structural variant as the most stable structure for Mg_3PN , Ca_3PN , Sr_3PN , Ba_3PN , and Zn_3PN from their corresponding E-V graphs. For representation, we have given E-V curves for Ca_3PN alone which is shown in Fig. 1. Since all the considered compounds stabilize in the same crystal structure, for representation we have given the ground state structure

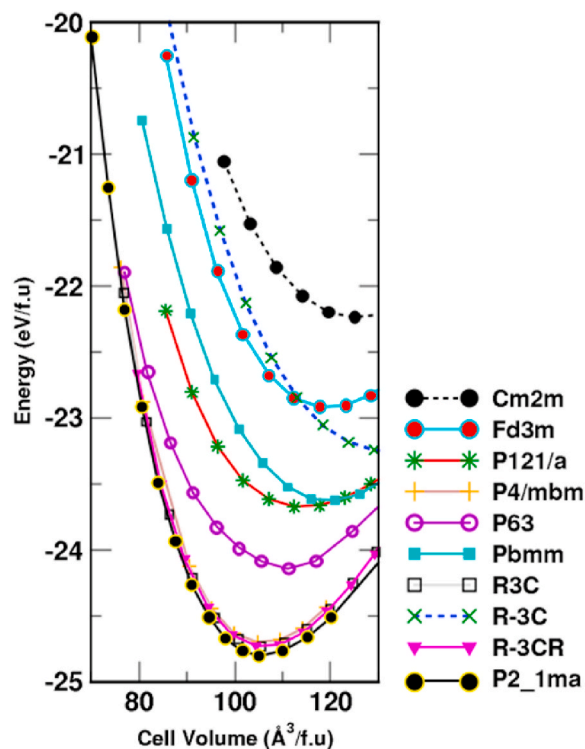


Fig. 1. Calculated cell volume vs free energy curves for Ca_3PN in different possible space groups.

for Ba_3PN alone here in Fig. 2. From this figure, we can get the information that in all these predicted compounds, nitrogen is in octahedral coordination with the corresponding alkali metal atoms. The optimized equilibrium lattice parameters, equilibrium volume, corresponding bulk modulus, and the Formation energy for the compounds are listed in Table 1. The details of positions of atoms in each compound are given in Table S1 in the supplementary information. The bulk modulus values of these compounds are calculated by fitting pressure-volume data to a third order Birch–Murnaghan equation of state [37]. The structural features of each compound and their stability are discussed as follows.

The structural, elastic and electronic properties of Mg_3PN compound were already done theoretically by Amara et al. [13] In 2013, by assuming hypothetical cubic structure with $\text{Pm}\bar{3}\text{m}$ space group using full-potential augmented plane wave plus local orbital (FP-LAPW + lo) method within the generalized gradient approximation based on PBEsol, Perdew 2008 functional [48]. In addition to the above, studies on the thermoelectric and optical properties for the cubic Mg_3PN compound were done using various exchange correlational potentials by Abdul Basit. et.al. However, in our optimization calculations for the Mg_3PN compound, the $P2_1ma$ (NaNbO_3) type orthorhombic structure is seen much lower than the cubic $\text{Pm}\bar{3}\text{m}$ (SrTiO_3) structure with an energy value of 0.823 eV/f.u.

From the prediction study done by Mochizuki et al. [29], using only 7 structural types as input in their structural optimization calculation, they found that this compound stabilizes in an orthorhombic structure with $Pbnm$ space group. But, from our detailed structural optimization calculation considering 32 structural variants as input in the structural optimization calculation we found that the total energy of Mg_3PN in the $P2_1ma$ (NaNbO_3) is 0.929 eV/f.u. lower than that of Mg_3PN in the $Pbnm$ (LaTiO_3) space group. So, we are unable to compare our results with their studies as the physical properties are sensitive to their ground state crystal structure. The bond angle of Mg-N-Mg , [Mg_6N] octahedra is found in the range 89.1° – 180° .

A distorted orthorhombic structure was already found and reported for the Ca_3PN compound in an earlier experimental study [15]. But the structural data for Ca_3PN is given as cubic $\text{Pm}\bar{3}\text{m}$ in the ICSD [49] Materials Project database [50], OQMD [51] and Jarvis [52] But according to Vasant. et.al. [24] and Mochizuki et al. [29], Ca_3PN stabilizes in a $Pbnm$ space group with orthorhombic symmetry. Excluding the lattice parameters, no other structural information such as atomic positions, bond distance, bond angle, etc. for the compound Ca_3PN in the

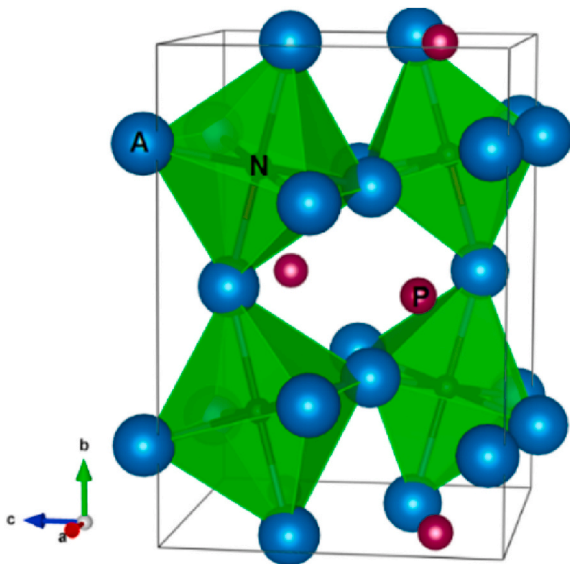


Fig. 2. The ground state crystal structures of (a) A_3PN ($\text{A} = \text{Mg}, \text{Ca}, \text{Sr}, \text{Ba}, \text{and Zn}$) in the orthorhombic phase with space group $P2_1ma$.

Table 1

The optimized equilibrium lattice parameters (a, b, c), Optimized equilibrium volume, formation energy, bulk modulus (B_0) and, band gap value (from HSE06) for A_3PN ($\text{A} = \text{Be}, \text{Mg}, \text{Ca}, \text{Sr}, \text{Ba}, \text{and Zn}$).

Compound (structure type; space group)	Unit cell parameters (Å)	Volume (\AA^3)	Formation Energy (kJ/mol)	B_0 (GPa)	Energy Band Gap (eV) (gap type)
Mg_3PN (NaNbO_3 ; $P2_1ma$)	$a = 5.9214$ $b = 8.3693$ $c = 5.9324$	72.82	-340.81	20.55	2.3 (direct)
Ca_3PN (NaNbO_3 ; $P2_1ma$)	$a = 6.7192$ (6.7091) $b = 9.4213$ (9.4518) $c = 6.6346$ (6.6581)	101.05	-492.22	15.48	2.1 (direct)
Sr_3PN (NaNbO_3 ; $P2_1ma$)	$a = 7.2870$ $b = 10.0875$ $c = 7.0490$	130.99	-400.31	11.80	1.7 (direct)
Ba_3PN (NaNbO_3 ; $P2_1ma$)	$a = 7.8377$ $b = 10.7371$ $c = 7.4021$	158.78	-255.30	8.49	1.1 (direct)
Zn_3PN (NaNbO_3 ; $P2_1ma$)	$a = 6.4054$ $b = 7.9235$ $c = 6.3636$	105.34	-430.84	18.05	0.5 (indirect)

$Pbnm$ space group have been reported in any literature. However, we found that the orthorhombic structured Ca_3PN is stabilized in the $P2_1ma$ space group [see Fig. 1] just like Mg_3PN . The involved energy difference between $P2_1ma$ (NaNbO_3) and LaTiO_3 ($Pbnm$) phase is 1.1 eV/f.u. We can see this difference from the E-V graph of Ca_3PN given in Fig. 1. Also, the energy involved for Ca_3PN in its equilibrium volume in the orthorhombic $P2_1ma$ (NaNbO_3) structure is 2.4 eV/f.u. lower than that in the cubic $\text{Pm}\bar{3}\text{m}$ (SrTiO_3) structure. It is pertinent to take notice of the fact that our equilibrium lattice parameters for Ca_3PN in the orthorhombic $P2_1ma$ (NaNbO_3) structure agree with what is obtained from the experimental XRD measurement. Our calculated Ca-N-Ca bond angles within each [Ca_6N] octahedra in the $P2_1ma$ (NaNbO_3) structure at the equilibrium volume vary from 89° to 180° , which are very much close to that of Mg_3PN .

The ground state crystal structures of Sr_3PN and Ba_3PN are also not yet determined experimentally. But, in the OQMD [51] and Jarvis [52] databases, the information about the electronic structure of hypothetical cubic ($\text{Pm}\bar{3}\text{m}$) phases of Sr_3PN and Ba_3PN are alone available. The involved energy values for the space group of $Pbnm$ are 0.992 eV/f.u. and 0.862 eV/f.u. higher than that of with $P2_1ma$ (NaNbO_3) for the respective compounds Sr_3PN and Ba_3PN . So, we can take the lowest energy configuration as the ground state crystal structure as $P2_1ma$ (NaNbO_3) with orthorhombic structure only. The calculated Sr-N-Sr bond angles within each [Sr_6N] octahedra are lying in the range of 88.3° – 180° . A similar type of distortion is also can be seen in the [Ba_6N] octahedra with Ba-N-Ba angle in the range of 87.3° – 179.1° .

Consistent with the other compounds, Zn_3PN also stabilize in an orthorhombic NaNbO_3 type structure with the $P2_1ma$ space group. It may be noted that there is no structural data available for this compound in any databases as well as in the literature. The calculated Zn-N-Zn bond angles within [Zn_6N] octahedra are varying between 74.7° and 155.3° indicating that this octahedra are highly distorted compared with that in other antiperovskites considered in the present study.

Since Zn is a transition metal element, there is always a possibility of having some different features for Zn_3PN compared to the remaining considered AE-based antiperovskites. The appearance of highly distorted octahedra is one of the notable features of Zn_3PN . Also, the

formation energy values for the predicted five compounds are obtained and reported the same in Table 1.

The formation energy of solids needs to be calculated to understand the degree of thermodynamic stability of the predicted solids [53,54]. We all know the equation of enthalpy of formation as $H = U + PV$ where, U is the internal energy and P, V are the pressure and volume respectively. The pressure-volume changes seem to be so small for solids at ambient temperatures and pressures and thus can be neglected for proceeding into further calculations. So, the enthalpy of formation will be considered only with internal energy change. By ignoring the effect of entropy contribution, the enthalpy of formation for A_3PN compounds can be estimated as:

$$\Delta H = E_{A_3PN} - (3E_A + E_P + E_N) \quad (1)$$

Where E_{A_3PN} , E_A , E_P and E_N are the total energy for A_3PN , A (=Mg, Ca, Sr, Ba and Zn) and Phosphorous and Nitrogen, respectively obtained from structural optimization. From the calculated heat of formation given in Table 1, it is clear that all these compounds are having negative heat of formation and hence they all will be stable at ambient condition in orthorhombic structure. Further it suggests that all these compounds can be synthesised experimentally.

3.2. Band structure analysis

The band structures of A_3PN compounds along the high-symmetry directions of $X \rightarrow \Gamma \rightarrow Y \rightarrow S$ in the irreducible part of the first Brillouin zone are given in Fig. 3. From this figure, it can be seen that the four compounds Mg_3PN , Ca_3PN , Sr_3PN , and Ba_3PN possess direct band gap behaviour with band gap values 1.1 eV, 1.7 eV, 2.1 eV, and 2.3 eV, respectively. But, for Zn_3PN compound, [Fig. 3(e)], the VBM is located along the Γ -Y direction and the CBM is located at the Γ point. Hence, we can understand that Zn_3PN is having indirect band behaviour with a small band gap value of 0.5 eV. Considering the indirect band behaviour with a very small bandgap value of Zn_3PN , one can conclude that this material is not suitable for higher efficiency solar cell application as it cannot harvest maximum energy from the solar spectrum and also phonon assisted optical transition alone possible. Because of our preference towards direct bandgap materials with optimum bandgap values starting from 1 eV to harvest maximum energy in the solar spectrum, we have discarded the indirect bandgap Zn_3PN compound from further analysis.

As we aim to get new compounds exhibiting excellent features applicable for higher efficiency TSC applications, four isoelectronic-isostructural potential compounds Mg_3PN , Ca_3PN , Sr_3PN and Ba_3PN are selected for the detailed analysis since they show various energy band gap values ranging from 1.1 eV to 2.3 eV. Also, the wide-band gap

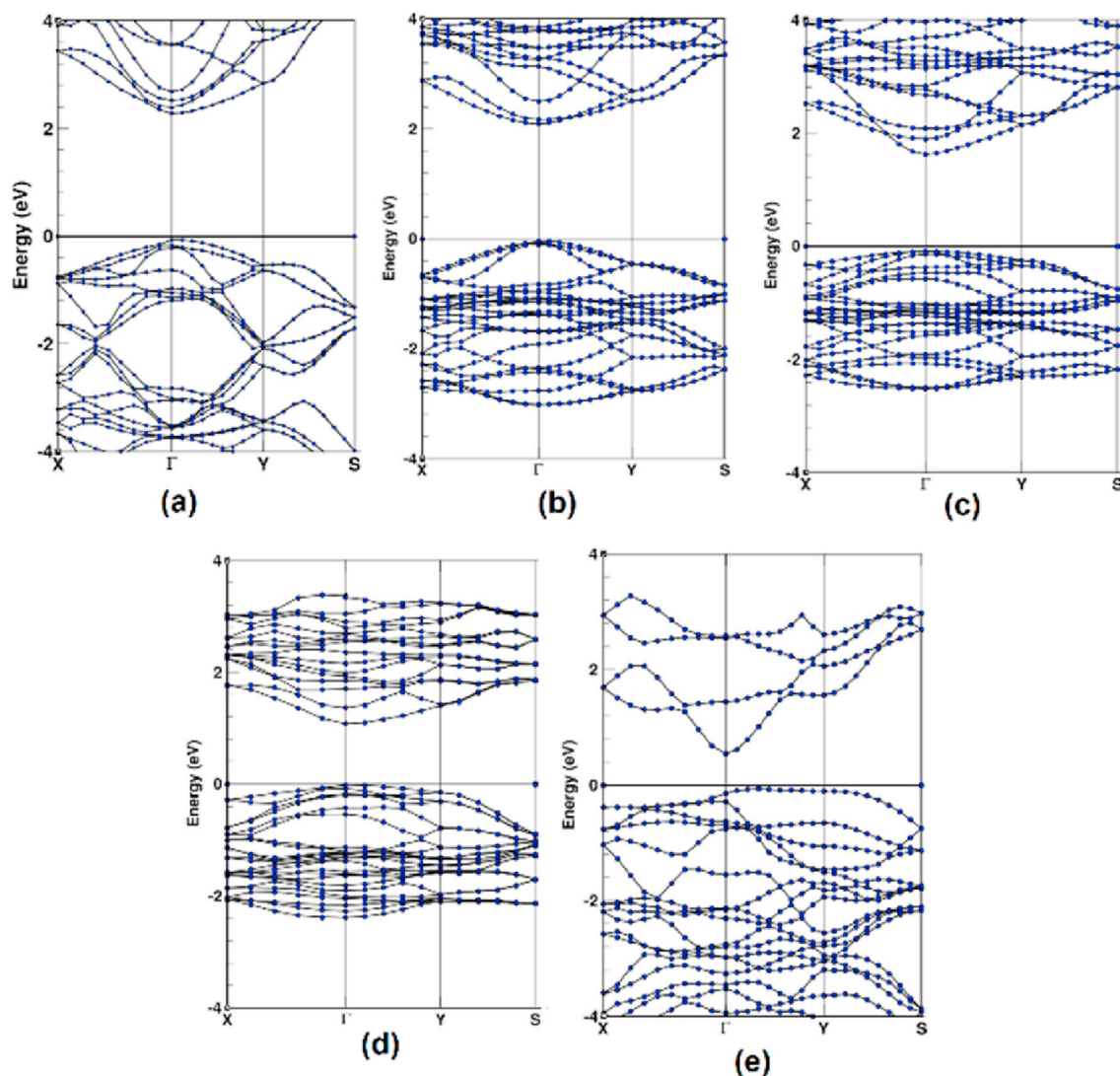


Fig. 3. Band structure (HSE06) of (a) Mg_3PN , (b) Ca_3PN , (c) Sr_3PN and (d) Ba_3PN and (e) Zn_3PN .

semiconductors Mg_3PN and Ca_3PN may be suitable for the application in solar water splitting where the bandgap needs to be in the range between 1.8 and 2.2 eV [55,56]. Also, these two compounds can be employed in efficient LED, and photonic devices [57,58].

3.2.1. Customizing the bandgap by making Sr substituted ($Ba_{3-x}Sr_xPN$) compounds

To harvest the maximum energy from solar spectrum, it is necessary to have more direct band gap materials with near-optimum band gap value (~1.52 eV). For that, we have systematically explored the possibilities for making solid solutions with the potential two compounds, Sr_3PN and Ba_3PN since they have band gap values of 1.1 eV and 1.7 eV respectively. As we are interested to find new compounds for photovoltaic application, we have customized the bandgap of Ba_3PN by substitution of Ba with different concentration of Sr in the pure system. By this substitution we have designed new compounds such as $BaSr_2PN$, $Ba_{1.5}Sr_{1.5}PN$, and Ba_2SrPN , and optimized their structure using total energy calculation. Thus, the obtained equilibrium structures were used to study their physical properties. Here we report the finding of strong solar absorption from our predicted strontium substituted compounds such as $BaSr_2PN$, $Ba_{1.5}Sr_{1.5}PN$, and Ba_2SrPN . The formation energy values and the HSE06 band gap values for these three compounds are reported in Table S2 in the supplementary information. Since these three compounds are also showing negative formation energy, we can confirm that they will be thermodynamically feasible to form.

The band structures of the newly predicted three compounds are given in Fig. S1(a), (b) and (c) respectively in the supplementary information. From these band structures, it is clear that the newly designed Sr-substituted compounds show direct bandgap behaviour with 1.27 eV, 1.12 eV, and 1.38 eV energy band gap values for $BaSr_2PN$, $Ba_{1.5}Sr_{1.5}PN$, and Ba_2SrPN respectively. The presence of well-dispersed bands in both the conduction band (CB) edge and valence band (VB) edge is another important feature considered when we made the above conclusion.

The minute-details of the nature of each band with respect to the k -path can only be described with the help of orbital projected band structure [59] and which is done by pVasp [46]. The orbital projected band analysis shows that the VBM for all these compounds are originating by electrons from p_x orbitals of nitrogen except Mg_3PN where the electrons from the p_x orbital of both N and P contributing equally. The CBM is contributed by the $d_{x^2-y^2}$ states of the AE elements ($A = Ca, Sr,$ and Ba) and is contributed from $Ba-d_{x^2-y^2}$ states for $BaSr_2PN$, $Ba_{1.5}Sr_{1.5}PN$, and Ba_2SrPN compounds. However, the CBM of Mg_3PN is mainly originating from the $2s$ and $2p$ orbitals of Mg with small contribution from the electronic states (s,p) of both P and N. Since the probability of creating electrons and holes is more in direct bandgap semiconductors during optical excitation since optical transitions are momentum conserving transitions, one can expect more carriers in these systems during optical excitation. For the compounds, as the VBM and the CBM are originating from different atomic sites, the chances of electron-hole association will become so less and make the charge carrier recombination rate lower.

There are some suitable features of seven antiperovskite compounds such as Mg_3PN , Ca_3PN , Sr_3PN , Ba_3PN , $BaSr_2PN$, $Ba_{1.5}Sr_{1.5}PN$, and Ba_2SrPN for using them as the absorbing layer in higher efficiency TSCs are given below:

1) Direct band gap nature and Bandgap Tunability

The advantage of having direct band gap nature for the above mentioned seven materials is that they can absorb sunlight efficiently without losing solar energy by thermal radiation. Apart from the direct band gap feature, the wide range of band gap values possessed by these predicted compounds make them more interesting to use in TSCs. One other relevant property of these A_3PN based antiperovskites for TSC is the tunability of their band gap values as demonstrated through the

detailed electronic structure analysis of $Ba_{3-x}Sr_xPN$.

According to the efficient tandem solar cell configuration, the topmost absorbing layer should contain a semiconductor with larger band gap value and the bottommost layer should have a semiconductor with smaller band gap value. The topmost layer semiconductor will absorb higher energy range of solar spectrum and will be transparent to the next stacked layer with lower energy band gap value than that of the top cell. In the current study, we can suggest the stacking of seven compounds in the descending order of the band gap; $Mg_3PN > Ca_3PN > Sr_3PN > Ba_2SrPN > BaSr_2PN > Ba_{1.5}Sr_{1.5}PN > Ba_3PN$ so that we can harvest most part of the solar spectrum efficiently.

2) Probability of less recombination rate between electron and holes

For all the compounds, the recombination rate between the carriers is expected to be so small since the photoexcited electrons and holes take their seats in two different atomic sites, that means they are well separated spatially from each other, and which is good for higher efficiency solar cells [60].

3.3. Chemical bonding analysis of Mg_3PN , Ca_3PN , Sr_3PN , Ba_3PN , $BaSr_2PN$, $Ba_{1.5}Sr_{1.5}PN$, and Ba_2SrPN

The density of states are calculated and plotted here for all the compounds for a better understanding of the chemical bonding interaction between the constituent elements. Also, the charge density analyses were made to visualize the bonding behaviour in these solids (see in Fig. 5). Incorporating these two analyses will give a clear understanding about the bonding character between the constituents

3.3.1. Density of states and orbital character analysis

Here, total density of states (TDOS) and partial density of states (PDOS) are given in separate figures for these compounds since the unit along the y-axis is different for both TDOS and PDOS. The TDOS for the compound Mg_3PN , Ca_3PN , Sr_3PN , Ba_3PN are given in the supplementary information in Fig. S2(a), (b), (c) and (d), respectively. Also, the TDOS plots for $BaSr_2PN$, $Ba_{1.5}Sr_{1.5}PN$, and Ba_2SrPN are given in Fig. S3 (a), (b) (c) respectively in the supplementary information.

For all the considered compounds, the role of its constituent atoms in VB and conduction band (CB) are analysed from the PDOS (see Fig. 4(a), (b), (c), (d), (e), (f)) of the compounds. Due to the isoelectronic and isostructural nature of both Ca_3PN and Sr_3PN , the TDOS distribution for the two compounds are also almost the same. So, we have done the PDOS analysis for Sr_3PN alone as a representative system.

The TDOS plots are given within an energy range from -14 eV to 6 eV. From the TDOS, we got the information that there are two distinct regions present in the valence band (VB) of Mg_3PN . But for Ca_3PN , and Sr_3PN , the VB has three distinct regions whereas, the VB is further split into four for Ba_3PN , and the Sr substituted compounds.

The lower energy regions in the VB are well localized and separated from the DOS at the higher energy region of the VB and hence they will not participate either for chemical bonding or for electrical conductivity and because of that so we have not considered those regions for the study. So, The PDOS plots are plotted within an energy range from -5 eV to 5 eV with Fermi level is set to zero.

For all the predicted compounds, the top of the valence bands composed of $P(3p)$ and $N(2p)$ states. But for Ba_3PN , Sr_3PN and three Sr-substituted compounds, in addition to these N/P(p) states, very small amount of contribution from the Ba, Sr($4p/5d$) states are also present in the top of the valence band. Also, it is also necessary to add that the VBM principally occur from the $N(2p)$ states for all the compounds.

Analysing the similarities in CBM, it is evident that the d orbitals of AE element mainly cause for the CBM for all the compounds except Mg_3PN , where CBM is dominated by both $Mg(2s)$ and $P(3s)$ states as evident from Fig. 4(a).

So, for all the compounds, the negligibly small contribution from the

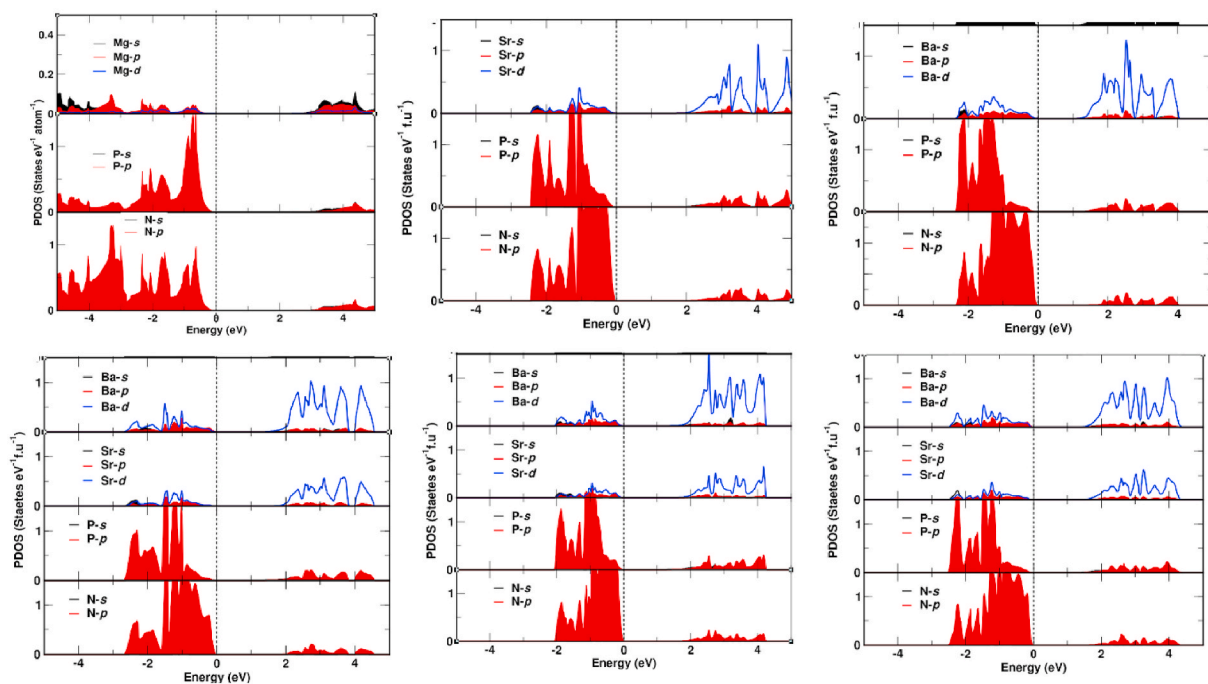


Fig. 4. The calculated partial densities of states for (a) Mg_3PN , (b) Sr_3PN , (c) Ba_3PN (d) BaSr_2PN (e) $\text{Ba}_{1.5}\text{Sr}_{1.5}\text{PN}$ and (f) Ba_2SrPN obtained from hybrid functional calculation. The Fermi level is set as zero.

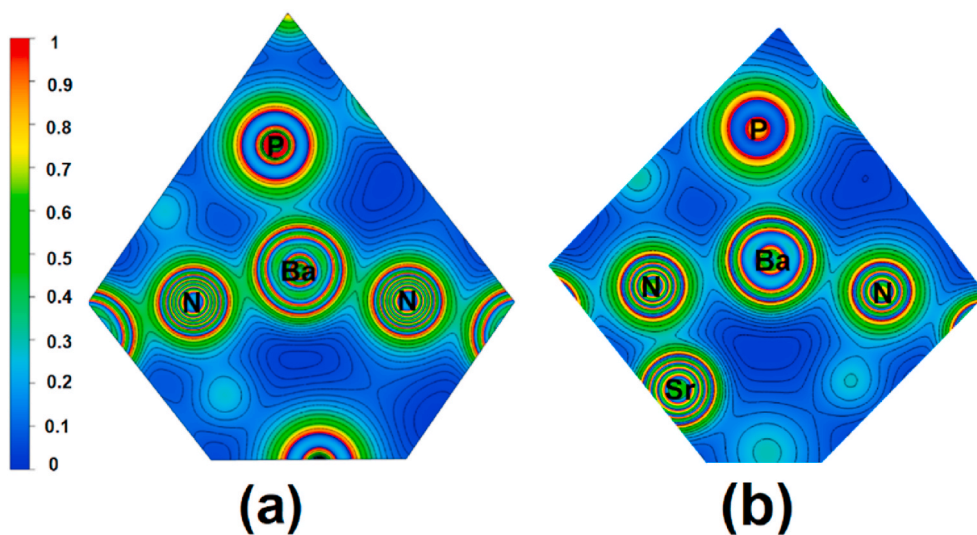


Fig. 5. (Colour Online) The charge density plot for (a) Ba_3PN and (b) $\text{Ba}_{1.5}\text{Sr}_{1.5}\text{PN}$ where the planes are selected in such a way that the Ba-N, Sr-N, Ba-P and Sr-P bonds are clearly.

AE element present in the VB clearly indicates the ionic interaction between of the corresponding AE with its neighbours. But the small contribution of (d/p) orbitals of the AE element and its hybridization with N/P- p orbitals in each compound leading to the presence of noticeable covalent bonding. Along with the energetical degeneracy, the spatially presence of AE atoms adjacent to N/P make noticeable covalent bonding, between AE-N as well as AE-P and this is clear in our charge density analysis which is described later. This partial covalency is a key for the dispersed bands in the vicinity of band edges and the semiconducting behaviour, and because of the presence of well-dispersed bands the charge carrier effective mass values are expected to be low, which in turn increase the carrier mobility and conductivity.

We can also see that the Sr substitution does not change much the electronic structure in the band edges significantly though it has shifted

them such that the bandgap values increase by Sr substitution.

Since the (AE) metals are electropositive and both N and P are electronegative, we have calculated the electronegativity difference between Mg-N, Mg-P, Ca-N, Ca-P, Sr-N, Sr-P, Ba-N and Ba-P and are 1.73, 0.88, 2.04, 1.19, 2, 1.2, 2.1, and 1.3, respectively. Due to this substantial electronegativity difference between the ions indicate the presence of ionic bonding between them. Due to this ionic interaction the s electrons from AE metals are almost transferred to both P and N and hence their contribution in the valence band is negligible. So, we can conclude that the bonding interaction between alkali metals with N/P is dominant ionic bonding with small covalency. This is pointing that these materials exhibit a mixed nature of ionic-covalent bonding.

3.3.2. Charge density analysis

We have visualized the bonding between the constituents for the compounds, Mg_3PN , Ca_3PN , Ba_3PN , Ba_2SrPN , $Ba_{1.5}Sr_{1.5}PN$, $BaSr_2PN$, and Sr_3PN using the VESTA [61] program. Since the charge density distribution for Mg_3PN , Ca_3PN , Sr_3PN , and Ba_3PN are almost the same, we have depicted the charge density for Ba_3PN as a representative valence electron charge-density in the planes where one could see the charge distribution system in Fig. 5(a). For the three Sr substituted compounds ($Ba_{3-x}Sr_xPN$) also the charge density distribution looks in the similar way, so we depicted the charge density only for $Ba_{1.5}Sr_{1.5}PN$ and which is given in Fig. 5(b).

Here we have selected planes in such a way that Ba–N, Ba–P, Sr–N, and Sr–P bonds are visible. From the charge density distribution of Ba_3PN , it is evident that there is spherically symmetric charge distribution at the Ba, P, and N sites with very small anisotropic charge distribution in the interstitial region clearly specifies the presence of ionic bonding between the constituents with small covalency. Moreover, the number of electrons at the N and P sites are larger than that in the corresponding neutral atom which affirms the presence of ionic bonding.

However, owing to the presence of hybridization interaction between Ba(5d) with N(2p) and P(3p) states as concluded from the DOS analysis, there is small non-spherical charge distribution present between Ba and N/P. This points out the presence of noticeable covalent bonding between Ba and N/P. One would also expect a similar type of ionic-covalent bonding nature between constituents in other antiperovskite compounds such as Mg_3PN , Ca_3PN , and Sr_3PN .

As we have seen from the charge density analysis of Ba_3PN , a similar bonding behaviour can also be seen for $Ba_{1.5}Sr_{1.5}PN$ (see in Fig. 5(b)). Here the noticeable amount of charge is present in the interstitial region between N/P and the A (A = Ba and Sr) site and it distributed anisotropically due to covalent hybridization. This hybridization is the clear indication of covalent bonding between N/P and A atoms. That means, in addition to the Ba–N covalent bonding, the sharing nature can be identified between Sr and N/P also. A similar type of hybridization between the constituents can also be seen for the other compositions in this series. And it is to be noted that the covalency between Sr–N is stronger compared to that of between Ba and N. This is mainly because of the low electronegativity difference between Sr and N compared to that between Ba and N [62].

Thus, as a part of the conclusion about the bonding nature, we can confidently say that these compounds show a mixed ionic-covalent bonding nature. This covalent hybridisation brings broad band features for the electronic states in the vicinity of the band edges. Due to these, well dispersed bands are formed at the band edges resulting the effective masses of the carriers relatively smaller which bring high carrier mobility and hence improve the efficiency of the solar cells if one makes such cell out of these materials.

3.4. Optical properties

The analysis of optical properties is a powerful tool to determine the overall band behaviour of a solid [43,63–68]. The optical properties can be obtained from the understanding of complex dielectric function $\epsilon(\omega) = \epsilon_1(\omega) + i\epsilon_2$. This complex dielectric function can tell the optical character of the medium at any photon energies. The imaginary part $\epsilon_2(\omega)$ of the dielectric function is directly related to the electronic band structure of a material and describes the absorptive behaviour. The optical properties are calculated at the equilibrium lattice constants for radiation up to 7 eV within PBE-GGA formalism. We have applied the artificial shift technique (scissor operation) for all the spectra in the considered compounds to correct for the DFT underestimation of band gaps. The rigid shift is done by considering the exact band gap values obtained from the HSE06 functional.

Since the compounds have orthorhombic symmetry ($a \neq b \neq c$), we need to consider the dielectric tensor in three directions ($\epsilon_{xx} \neq \epsilon_{yy} \neq \epsilon_{zz}$),

which can fully determine the linear optical properties. Once the imaginary part of the complex dielectric function is determined, then we can calculate the corresponding real part using Kramers - Kronig relations [69,70] and then can compute the other optical constants.

In our previous studies [65], we have explained the structural, electronic, and optical properties of Ca_3PN in the cubic $Pm\bar{3}m$ structure. But, in the current study, we have predicted an orthorhombic structure with the space group of $P2_1ma$ ($NaNbO_3$) as the ground state crystal structure for Ca_3PN . So, it is necessary to explain the structural distortions with respect to the optical anisotropy for this orthorhombic Ca_3PN compound. The plots of $\epsilon_2(\omega)$ spectra for the orthorhombic Ca_3PN (in $P2_1ma$) and the cubic Ca_3PN ($Pm\bar{3}m$) are portrayed in Fig. S4 (a) and (b) respectively in the supplementary information. The $\epsilon_2(\omega)$ spectra for the Ca_3PN compound in the two different structures are further analysed and compared each other in the supplementary information in section 1.

The absorption coefficient is the important parameter to consider which is given in Fig. 6(a). This is the parameter which gives the length travelled by a photon into the material before it is completely absorbed. The non-zero part in all absorption spectra indicates that the energy at which the absorption starts, in other words, it is the band gap values of each material. The optical absorption in the lower energy range is mainly arising from the interband transition of electrons from the topmost valence band to the lowest conduction band. The other peaks observed in $\alpha(\omega)$ spectra may not be due to the transitions of electrons from VBM to CBM but may come from the lower energy region of the VB to the CB. By analysing the $\alpha_{ave}(\omega)$ spectra we can infer that the light absorption performance of these materials, is reasonably high in the visible region and it is in the order of 10^5 cm^{-1} for all these compounds.

Due to increase in the bandgap value when one goes from Ba_3PN to Mg_3PN , the optical absorption spectra also shifting systematically towards higher energy. In all these compounds there is a peak in the absorption spectra and this peak position also shifting systematically when one goes across this series. This feature is advantageous to build TSC using these materials as different layers will have maximum optical absorption in a different energy range of the solar spectrum and thus will

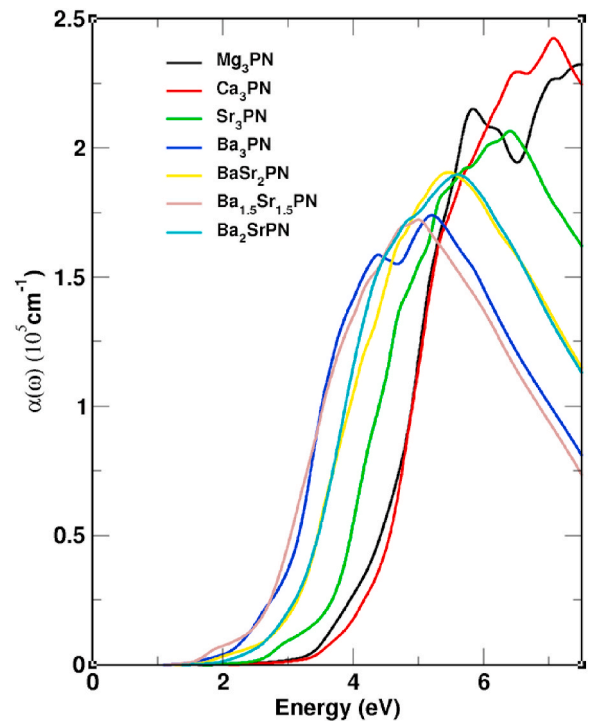


Fig. 6. (a) The calculated optical spectra of Average of absorption coefficients ($\alpha_{ave}(\omega)$) along the three axes of the seven compounds such as Mg_3PN , Ca_3PN , Sr_3PN , Ba_3PN , $BaSr_2PN$, $Ba_{1.5}Sr_{1.5}PN$, and Ba_2SrPN .

have high PCE. Even though the absorption is high in the visible region, more elevated intensity peaks are observed in the ultraviolet (UV) region for all the compounds. So, not only these materials are useful for PV applications, but also can be used as the possible shields for UV radiation. It is interesting to analyse the origin of absorption edge so that one can tune their optoelectronic properties and hence we made the analysis as follows. Let us first consider Mg_3PN where the absorption edge originating from the interband electronic transition from the occupied p states of both N and P to unoccupied $Mg(s)$. However, in the other compounds the absorption edge originates by the excitation of electrons from their $N(2p)$ states to the d states of the corresponding AE site. In the Sr substituted compounds such as $BaSr_2PN$, $Ba_{1.5}Sr_{1.5}PN$, and Ba_2SrPN , the optical absorption edge originates from $N(2p)$ states in the VBM to $Ba-d$ states in the CBM.

Let us now analyse the imaginary part of the complex refractive index, i.e. extinction coefficient, $[k(\omega)]$ (given in Fig. S5(b) in the supplementary information) for the compounds. If we compare the extinction coefficient spectrum with the corresponding absorption coefficient, in both cases there are two distinct peaks in each compound. However, in the case of $\alpha_{ave}(\omega)$ spectra, the low energy peak is having low intensity than the higher energy peak and in contrast, the $k_{ave}(\omega)$ spectra at the higher energy peak is having higher intensity than the lower energy peak. Moreover, in the $\alpha_{ave}(\omega)$ spectra, Ba_3PN is having lower intensity and Mg_3PN is having higher intensity.

But, in the $k_{ave}(\omega)$ spectra is having almost the same value in the maximum intensity for all the compounds considered here as shown in It may be noted that the energy position of the two peaks in each compound in the $\alpha_{ave}(\omega)$ and $k_{ave}(\omega)$ spectra are the same though their intensity gets altered. The optical conductivity is an optical phenomenon that illustrates that the conductivity of a material with the absorption of radiation. The $\sigma_{2(ave)}(\omega)$ spectrum for Mg_3PN , Ca_3PN , Sr_3PN , Ba_3PN , $BaSr_2PN$, $Ba_{1.5}Sr_{1.5}PN$, Ba_2SrPN are shown in Fig.S(5) (c) in the supplementary information. The frequency-dependent features of $\sigma_{2ave}(\omega)$ spectra for the compounds look almost similar to the features of $\alpha_{ave}(\omega)$ spectra with two distinct peaks. It can be noted that all the compounds have comparatively high $k_{ave}(\omega)$ and $\sigma_{2ave}(\omega)$ values in the visible energy region.

In the optical reflectivity average spectra, $R_{ave}(\omega)$ for the compounds are displayed in Fig. S(5) (d) in the supplementary information. For all the compounds, the $R_{ave}(\omega)$ spectra show reflectivity which are less than 20% in the lower energy range around 2 eV. This indicates that these compounds are capable of allowing the lower energy photons (<2 eV) to pass through them. It is also worth noting that for all the compounds though they have low reflectivity in the visible part of the solar spectrum, their reflectivity value increases continuously in the UV range. From the above optical property analysis, we can conclude that these antiperovskites can be used as good solar light absorbers in the higher efficient TSCs because of their advantageous properties such as high absorption coefficients, high extinction coefficients and high optical conductivity along with small reflectance in the visible energy region.

3.5. Carrier effective mass and carrier mobility

The charge carrier effective mass [71,72] is an important physical quantity to account the understanding of the mobility of the charge carriers and hence obviously one can evaluate the photovoltaic performance of solar cell materials [65].

We have tried reproducing the effective mass values with VASPKIT for some of the compounds for which the results are already available in the existing literature [73,74]. The reliability of this method is quite satisfactory [65]. We have calculated the band structure using hybrid functional with a higher number of k -points in the high symmetric directions around the band edges to get more accurate value of the effective mass of charge carriers.

The mobility of charge carriers in semiconductors is inversely proportional to their corresponding effective mass values. There is a rela-

tionship between the charge mobility and the charge carrier effective mass which is given in the following equation:

$$\mu = \frac{\tau}{m^*} \quad (2)$$

where μ is the charge mobility, e is the electronic charge, τ is the collision time, and m^* is the effective mass. It may be noted that the effective mass of the carrier depends on the curvature of the band and if the band is dispersed, then the effective mass will be low and if it is flat then the effective mass will be high. Our results of the hole and electron effective masses on the corresponding VB and CB edges along two different crystallographic directions, $\Gamma \rightarrow X$ and $\Gamma \rightarrow Y$, for the seven concerned antiperovskites Mg_3PN , Ca_3PN , Sr_3PN , Ba_3PN , $BaSr_2PN$, $Ba_{1.5}Sr_{1.5}PN$, Ba_2SrPN are listed in Table 2.

The results reported in Table 2 are satisfying to the concept that the low effective mass of charge carriers can lead to well-dispersed bands.

For the two compounds Mg_3PN and Ca_3PN , the dispersion of bands in the VBM along $\Gamma \rightarrow X$ direction is more than that in their corresponding CBM.

Agreeing with the above, the reported hole effective mass values are lower than the corresponding electron effective mass values for the compounds. Just opposite to the above, the VBM along $\Gamma \rightarrow X$ direction look more flatter than their corresponding CBM, thus implies that the electron effective mass values are lower compared to the hole effective masses for the remaining compounds, Sr_3PN , Ba_3PN , Ba_2SrPN , $Ba_{1.5}Sr_{1.5}PN$ and $BaSr_2PN$.

Now, analysing the band dispersion of VBM and CBM along $\Gamma \rightarrow Y$ direction, we can understand that, for all compounds, the CBM is more broadly dispersed than the corresponding VBM. Consequently, we are able to achieve much lower effective mass values along the $\Gamma \rightarrow Y$ direction, which are very small than the hole effective masses.

It is reported in literatures that, we can expect high charge carrier mobility when the effective mass of a charge carrier is lower than $0.5m_0$ in at least one of the crystallographic direction (where m_0 is the electron mass) [55,60]. For most of the considered compounds, both the electron and hole effective mass values are lower than $0.5m_0$ along at least one of the considered directions. This inferred that the solar cell can be made out of these compounds will have high carrier mobility and hence the charge separation will be efficient that will increase the photo conversion efficiency.

It has already been reported that the parameter of recombination can also be determined by taking the ratio of the charge carrier effective masses in the VBM and CBM [60].

$$D = \frac{m_e}{m_h} \quad (3)$$

When this D value is high, then we can expect a large distance between the electron and hole and in such case the probability of electrons and holes coming closer will be less [60]. Among the considered compounds, the highest D value is obtained for Mg_3PN and Ca_3PN along the $\Gamma \rightarrow X$ direction where both the hole and electron effective masses are very low. The high D value along with low charge carrier effective mass values makes these materials more attractive to use as absorber layers in high efficiency TSCs.

4. Exciton binding energy

Excitonic binding energy is another parameter relevant in photovoltaic applications. The free charge carriers can be collected for conduction only after separating the electron-hole pair (exciton). So, the energy demanded for this electron-hole detachment is usually named as excitonic binding energy. Even though, the binding energy of excitons is very small for non-excitonic solar cells compared to that of excitonic-solar cells, it is necessary to prove the statement with our results. If the binding energy of excitons is small, then the exciton can be dissociated easily by thermally or by potential gradient. As a result, the

Table 2

The calculated carrier effective masses for the electrons (m_e^*), holes (m_h^*) at the band edges, Static dielectric constant, Exciton binding energy values for Mg₃PN, Ca₃PN, Sr₃PN, Ba₃PN, BaSr₂PN, Ba_{1.5}Sr_{1.5}PN, and Ba₂SrPN in two crystallographic directions.

Compound	$\Gamma \rightarrow X$				$\Gamma \rightarrow Y$			
	$m_h (m_0)$	$m_e (m_0)$	Static Dielectric Constant ($\epsilon_s^{(1,0,0)}$)	Exciton Binding Energy (E_b)	$m_h (m_0)$	$m_e (m_0)$	Static Dielectric Constant ($\epsilon_s^{(0,1,0)}$)	Exciton Binding Energy (E_b)
Mg ₃ PN	0.11	0.421	8.01	15	0.787	0.522	7.71	52
Ca ₃ PN	0.235	0.362	7.65	33	0.689	0.534	7.49	73
Sr ₃ PN	0.665	0.145	7.80	27	1.765	0.222	7.46	48
Ba ₃ PN	0.462	0.211	9.38	22	1.246	0.440	8.75	58
Ba ₂ SrPN	2.892	0.169	8.71	29	0.271	0.204	8.76	21
Ba _{1.5} Sr _{1.5} PN	0.734	0.125	9.00	18	2.812	0.131	8.80	22
BaSr ₂ PN	3.475	0.217	8.04	43	0.202	0.124	8.79	14

charge carriers can be collected for conduction which further enhances the carrier mobility. The exciton binding energy is obtained by the Wannier–Mott formula [75].

$$E_b = \frac{m_e m_h R_y}{m_0 (m_e + m_h) \epsilon_s^2} \quad (4)$$

where m_h , m_e are the effective masses of holes and electrons, respectively. R_y is the Rydberg constant, and ϵ_s is the static dielectric constant. The excitonic binding energy values for each compound is calculated and reported in Table 2.

Moreover, it has been said that the materials with very low excitonic binding energy, especially less than 130 meV are more suitable for photovoltaic applications [76,77]. For all the compounds predicted here, the excitonic binding energy values are very small and less than 130 meV and thus they can be applied for PV applications.

5. Conclusion

In summary, we have operationalised an accurate method of structural optimization by considering 32 similar available crystal structures for designing new antiperovskite materials. Based on the systematic investigation, seven compounds contain earth-abundant and non-toxic elements such as Mg₃PN, Ca₃PN, Sr₃PN, Ba₃PN, BaSr₂PN, Ba_{1.5}Sr_{1.5}PN, and Ba₂SrPN have been selected with their key parameters related with solar cell applications. Since the considered seven compounds are isoelectronic and having iso-structural orthorhombic ground state structure with same space group $P2_1ma$ (NaNbO₃) with similar chemical bonding, the stacking of each sub cell will be easier. All the seven compounds attain direct band gap behaviour with band gap values ranging from 1.1 eV to 2.3 eV. One of the other relevant properties of these A₃PN based antiperovskites to use in higher efficiency TSC is the tunability of their band gap values as demonstrated through the detailed electronic structure analysis of Ba_{3-x}Sr_xPN. From the site and orbital projected band structure and DOS analysis we found that the possibility of recombination of the charge carriers will be minimal for all these systems since the photogenerated electrons and holes will be spatially separated as they reside in two different atoms. The noticeable presence of covalent bonding along with s/p electron band characters near the band edges brings broad band features for the electronic states at the band edges. Due to the formation of well dispersed bands at the band edges resulting in smaller effective masses of the carriers ($<0.5m_0$) which bring higher carrier mobility and hence increase the charge separation that improve the efficiency of the solar cells if one makes such cell out of these materials. The excitonic binding energy is found to be so small, say less than 130 eV for all the predicted compounds, which can help in collecting the charge carriers for conduction. The high optical absorption coefficient, high extinction coefficient, and high optical conductivity with low reflectivity in the visible region implying that these compounds are potential materials to use as the absorbing layers in TSCs applications.

From the above conclusions, it is beyond doubt that one can make higher efficiency tandem solar cell where the top layer will be Mg₃PN and the bottommost layer will be Ba₃PN with the rest of the compounds as the intermediate layers. We can expect that the experimentalists will definitely try synthesizing these predicted compounds and build high efficiency TSCs in not-so-distant future.

CRedit authorship contribution statement

P.D. Sreedevi: Writing – original draft, Visualization, Investigation, Formal analysis, Data curation. **R. Vidya:** Writing – review & editing, Validation, Conceptualization. **P. Ravindran:** Writing – review & editing, Supervision, Conceptualization.

Declaration of competing interest

The authors declare that they have no known competing financial interests or personal relationships that could have appeared to influence the work reported in this paper.

Acknowledgments

The authors would like to thank This research was supported by the Indo-Norwegian Cooperative Program (INCP) via Grant No. F. No. 5812/2014(IC) and Department of Science and Technology, India via Grant No. SR/NM/NS1123/2013. P. R. likes to thank the CSIR for providing the financial support through EMR-II project-03(1398).

P. D. S. is grateful to the Department of Medical Physics, Anna University, Chennai for hospitality and also would like to thank Dr. Lokanath Patra and Dr. P. A. Damodaran for the critical reading of the manuscript.

The crystal structure and the charge density plots given in this article were portrayed using VESTA [61].

Appendix A. Supplementary data

Supplementary data to this article can be found online at <https://doi.org/10.1016/j.mssp.2022.106727>.

References

- [1] L.K. Ono, Y. Qi, S.(Frank) Liu, Progress toward stable lead halide perovskite solar cells, *Joule* 2 (2018) 1961–1990, <https://doi.org/10.1016/j.joule.2018.07.007>.
- [2] H.J. Queisser, Detailed balance limit for solar cell efficiency, *Mater. Sci. Eng., B.* 159–160 (2009) 322–328, <https://doi.org/10.1016/j.mseb.2008.06.033>.
- [3] Z. Zhang, Z. Li, L. Meng, S.Y. Lien, P. Gao, Perovskite-based tandem solar cells: get the most out of the sun, *Adv. Funct. Mater.* 30 (2020), <https://doi.org/10.1002/adfm.202001904>.
- [4] C. Shi, H. Yu, Q. Wang, L. Ye, Z. Gong, J. Ma, J. Jiang, M. Hua, C. Shuai, Y. Zhang, H. Ye, Hybrid organic–inorganic antiperovskites, *Angew. Chem.* 132 (2020) 173–177, <https://doi.org/10.1002/ange.201908945>.
- [5] M. Bilal, S. Jalali-Asadabadi, R. Ahmad, I. Ahmad, Electronic properties of antiperovskite materials from state-of-the-art density functional theory, *J. Chem.* 2015 (2015), <https://doi.org/10.1155/2015/495131>.

- [6] S.J.G.N. Petzow, F. Aldinger, Beryllium and beryllium compounds, Ullmann's Encycl. Ind. Chem. (2005), <https://doi.org/10.1002/14356007.a04>.
- [7] E.O. Chi, W.S. Kim, N.H. Hur, D. Jung, New Mg-based antiperovskites PnNMg_3 (Pn = As, Sb), Solid State Commun. 121 (2002) 309–312, [https://doi.org/10.1016/S0038-1098\(02\)00011-X](https://doi.org/10.1016/S0038-1098(02)00011-X).
- [8] T. Belaroussi, T. Benmessabih, F. Hamdache, B. Amrani, First-principles study of the structural and thermodynamic properties of AsNMg_3 antiperovskite, Phys. B. 403 (2008) 2649–2653, <https://doi.org/10.1016/j.physb.2008.01.047>.
- [9] A. Bouhemadou, R. Khenata, M. Chegaar, S. Maabed, First-principles calculations of structural, elastic, electronic and optical properties of the antiperovskite AsNMg_3 , Phys. Lett. A. 371 (2007) 337–343, <https://doi.org/10.1016/j.physleta.2007.06.030>.
- [10] I.R. Shein, A.L. Ivanovskii, Electronic band structure and chemical bonding in the new antiperovskites AsNMg_3 and SbNMg_3 , J. Solid State Chem. 177 (2004) 61–64, [https://doi.org/10.1016/S0022-4596\(03\)00309-8](https://doi.org/10.1016/S0022-4596(03)00309-8).
- [11] C.M.I. Okoye, First-principles optical calculations of AsNMg_3 and SbNMg_3 , Mater. Sci. Eng., B. 130 (2006) 101–107, <https://doi.org/10.1016/j.mseb.2006.02.066>.
- [12] A. Bouhemadou, R. Khenata, Ab initio study of the structural, elastic, electronic and optical properties of the antiperovskite SbNMg_3 , Comput. Mater. Sci. 39 (2007) 803–807, <https://doi.org/10.1016/j.commatsci.2006.10.003>.
- [13] K. Amara, M. Zemouli, M. Elkourti, A. Belfedal, F. Saadaoui, First-principles study of XNMg_3 (X = P, As, Sb and Bi) antiperovskite compounds, J. Alloy. Computd. 576 (2013) 398–403, <https://doi.org/10.1016/j.jallcom.2013.06.003>.
- [14] A. Basit, S. Ayaz Khan, G. Murtaza, A. Mehmood, R. Khenata, S. Bin Omran, M. Yaseen, Electronic, optical and thermoelectric properties of XNMg_3 (X = P, As, Sb, Bi) compounds, Mater. Sci. Semicond. Process. 43 (2016) 69–74, <https://doi.org/10.1016/j.mssp.2015.12.001>.
- [15] P.Y. Ming Chern, D.A. Vennos, F.J. DiSalvo, Synthesis, structure, and properties of anti-perovskite nitrides A-f, J. Solid State Chem. 96 (1992) 415–425. <http://www.dtic.mil/dtic/tr/fulltext/u2/a236589.pdf>.
- [16] M. Bilal, B. Khan, H.A. Rahnamaye Aliabad, M. Maqbool, S. Jalai Asadabadi, I. Ahmad, Thermoelectric properties of SbNca_3 and BiNca_3 for thermoelectric devices and alternative energy applications, Comput. Phys. Commun. 185 (2014) 1394–1398, <https://doi.org/10.1016/j.cpc.2014.02.001>.
- [17] M. Bilal, I. Ahmad, H.A. Rahnamaye Aliabad, S. Jalali Asadabadi, Detailed DFT studies of the band profiles and optical properties of antiperovskites SbNca_3 and BiNca_3 , Comput. Mater. Sci. 85 (2014) 310–315, <https://doi.org/10.1016/j.commatsci.2013.12.035>.
- [18] M. Bilal, I. Ahmad, S.J. Asadabadi, R. Ahmad, M. Maqbool, Thermoelectric properties of metallic antiperovskites AXD_3 (A = Ge, Sn, Pb, Al, Zn, Ga; X = N, C; D = Ca, Fe, Co), Electron. Mater. Lett. 11 (2015) 466–480, <https://doi.org/10.1007/s13391-015-4425-2>.
- [19] D.A. Papaconstantopoulos, W.E. Pickett, Ternary nitrides BiNca_3 and PbNca_3 : unusual ionic bonding in the antiperovskite structure, Phys. Rev. B 45 (1992) 4008–4012, <https://doi.org/10.1103/PhysRevB.45.4008>.
- [20] K. Haddadi, A. Bouhemadou, L. Louail, S. Maabed, D. Maoche, Structural and elastic properties under pressure effect of the cubic antiperovskite compounds ANca_3 (A = P, As, Sb, and Bi), Phys.Lett.A. 373 (2009) 1777–1781, <https://doi.org/10.1016/j.physleta.2009.03.016>.
- [21] M. Moakafi, R. Khenata, A. Bouhemadou, F. Semari, A.H. Reshak, M. Rabah, Elastic, electronic and optical properties of cubic antiperovskites SbNca_3 and BiNca_3 , Comput. Mater. Sci. 46 (2009) 1051–1057, <https://doi.org/10.1016/j.commatsci.2009.05.011>.
- [22] K. Haddadi, A. Bouhemadou, L. Louail, Y. Medkour, Structural, elastic and electronic properties of XNca_3 (X = Ge, Sn and Pb) compounds, Solid State Commun. 149 (2009) 619–624, <https://doi.org/10.1016/j.ssc.2009.01.025>.
- [23] K. Haddadi, A. Bouhemadou, L. Louail, Structural, elastic and electronic properties of the hexagonal anti-perovskites SbNBa_3 and BiNBa_3 , Comput. Mater. Sci. 48 (2010) 711–718, <https://doi.org/10.1016/j.commatsci.2010.03.015>.
- [24] P. Vansant, P. Van Camp, V. Van Doren, J. Martins, Variable-cell-shape-based structural optimization applied to calcium nitrides, Phys. Rev. B 57 (1998) 7615–7620, <https://doi.org/10.1103/PhysRevB.57.7615>.
- [25] S. Iqbal, G. Murtaza, R. Khenata, A. Mahmood, A. Yar, M. Muzammil, M. Khan, Electronic and optical properties of Ca_3MN (M = Ge, Sn, Pb, P, as, Sb and Bi) antiperovskite compounds, J. Electron. Mater. 45 (2016) 4188–4196, <https://doi.org/10.1007/s11664-016-4563-9>.
- [26] M.Y. Chern, F.J. Disalvo, J.B. Parise, J.A. Goldstone, The structural distortion of the anti-perovskite nitride Ca_3AsN , J. Solid State Chem. 96 (1992) 426–435, [https://doi.org/10.1016/S0022-4596\(05\)80277-4](https://doi.org/10.1016/S0022-4596(05)80277-4).
- [27] P.R. Vansant, P.E. Van Camp, V.E. Van Doren, J.L. Martins, AsNca_3 at high pressure, Comput. Mater. Sci. 10 (1998) 298–301, [https://doi.org/10.1016/s0927-0256\(97\)00101-8](https://doi.org/10.1016/s0927-0256(97)00101-8).
- [28] F. Gäbler, M. Kirchner, W. Schnelle, U. Schwarz, M. Schmitt, H. Rosner, R. Niewa, $(\text{Sr}_3\text{N})\text{E}$ and $(\text{Ba}_3\text{N})\text{E}$ (E = Sb, Bi): synthesis, crystal structures, and physical properties, Z. Anorg. Allg. Chem. 630 (2004) 2292–2298, <https://doi.org/10.1002/zaac.200400256>.
- [29] Y. Mochizuki, H.J. Sung, A. Takahashi, Y. Kumagai, F. Oba, Theoretical exploration of mixed-anion antiperovskite semiconductors M_3XN (M = Mg, Ca, Sr, Ba; X = P, As, Sb, Bi), Phys. Rev. Mater. 4 (2020) 1–14, <https://doi.org/10.1103/PhysRevMaterials.4.044601>.
- [30] D.M. Hoat, Structural, optoelectronic and thermoelectric properties of antiperovskite compounds Ae_3PbS (Ae = Ca, Sr and Ba): a first principles study, Phys.Lett.A. 383 (2019) 1648–1654, <https://doi.org/10.1016/j.physleta.2019.02.013>.
- [31] J. Dai, M.G. Ju, L. Ma, X.C. Zeng, $\text{Bi}(\text{Sb})\text{Nca}_3$: expansion of perovskite photovoltaics into all-inorganic anti-perovskite materials, J. Phys. Chem. C 123 (2019) 6363–6369, <https://doi.org/10.1021/acs.jpcc.8b11821>.
- [32] Q. Mahmood, A. Ashraf, M. Hassan, Investigations of optical and thermoelectric response of direct band gap Ca_3XO (X = Si, Ge) anti-perovskites stabilized in cubic and orthorhombic phases, Indian J. Phys. 92 (2018) 865–874, <https://doi.org/10.1007/s12648-018-1177-5>.
- [33] P.E. Blöchl, Projector augmented- wave method, Phys. Rev. B 50 (1994) 17953–17979, <https://doi.org/10.1103/PhysRevB.50.17953>.
- [34] G. Kresse, J. Hafner, Ab initio molecular dynamics for liquid metals, Phys. Rev. B 47 (1993) 558–561, <https://doi.org/10.1103/PhysRevB.47.558>.
- [35] J.P. Perdew, K. Burke, M. Ernzerhof, Generalized gradient approximation made simple, Phys. Rev. Lett. 77 (1996) 3865–3868, <https://doi.org/10.1103/PhysRevLett.77.3865>.
- [36] J.D. Pack, H.J. Monkhorst, Special points for Brillouin-zone integrations, Phys. Rev. B 13 (1976) 5188–5192, <https://doi.org/10.1103/PhysRevB.13.5188>.
- [37] F.D. Murnaghan, The compressibility OF media under extreme pressures, Proc. Natl. Acad. Sci. U.S.A. 30 (1944) 244–247, [https://doi.org/10.1016/s0016-0032\(24\)90498-4](https://doi.org/10.1016/s0016-0032(24)90498-4).
- [38] T.M. Henderson, J. Paier, G.E. Scuseria, Accurate treatment of solids with the HSE screened hybrid, Phys. Status Solidi B 248 (2011) 767–774, <https://doi.org/10.1002/pssb.201046303>.
- [39] M. Nolan, S. Grigoleit, D.C. Sayle, S.C. Parker, G.W. Watson, Density functional theory studies of the structure and electronic structure of pure and defective low index surfaces of ceria, Surf. Sci. 576 (2005) 217–229, <https://doi.org/10.1016/j.susc.2004.12.016>.
- [40] S. Kiruthika, H. Fjellvåg, P. Ravindran, Amphoteric behavior of hydrogen (H+1 and H-1) in complex hydrides from van der Waals interaction-including ab initio calculations, J. Mater. Chem. A. 7 (2019) 6228–6240, <https://doi.org/10.1039/c8ta11685g>.
- [41] S.Z. Karazhanov, P. Ravindran, H. Fjellvåg, B.G. Svensson, Electronic structure and optical properties of ZnSiO_3 and Zn_2SiO_4 , J. Appl. Phys. 106 (2009), <https://doi.org/10.1063/1.3268445>.
- [42] S. Saha, T.P. Sinha, A. Mookerjee, Electronic structure, chemical bonding, and optical properties of paraelectric BaTiO_3 , Phys. Rev. B 62 (2000) 8828–8834, <https://doi.org/10.1103/PhysRevB.62.8828>.
- [43] R. Ahuja, O. Eriksson, P. James, B. Johansson, Magnetic, optical, and magneto-optical properties of mnx (x = as, sb, or bi) from full-potential calculations, Phys. Rev. B 59 (1999) 15680–15693, <https://doi.org/10.1103/PhysRevB.59.15680>.
- [44] F. Wooten, Optical Properties of Solids, Acad. Press, 2013, [https://doi.org/10.1002/1521-3951\(200201\)229:1<611::AID-PSSB611>3.0.CO;2-3](https://doi.org/10.1002/1521-3951(200201)229:1<611::AID-PSSB611>3.0.CO;2-3).
- [45] P. Ravindran, A. Delin, R. Ahuja, B. Johansson, S. Auluck, J. Wills, O. Eriksson, Optical properties of monoclinic Sn from relativistic first-principles theory, Phys. Rev. B 56 (1997) 6851–6861, <https://doi.org/10.1103/PhysRevB.56.6851>.
- [46] O. Dubay, P4vasp, 2018.
- [47] V. Wang, Cover Page, VASPKIT, a Post-Processing Tool Ab-Initio Code VASP, 2009.
- [48] J.P. Perdew, A. Ruzsinszky, G.I. Csonka, O.A. Vydrov, G.E. Scuseria, L. A. Constantin, X. Zhou, K. Burke, Restoring the density-gradient expansion for exchange in solids and surfaces, Phys. Rev. Lett. 100 (2008) 2–6, <https://doi.org/10.1103/PhysRevLett.100.136406>.
- [49] G. Bergerhoff, R. Hundt, R. Sievers, I.D. Brown, The inorganic crystal structure data base, J. Chem. Inf. Comput. Sci. 23 (1983) 66–69, <https://doi.org/10.1021/ci00038a003>.
- [50] A. Jain, S.P. Ong, G. Hautier, W. Chen, W.D. Richards, S. Dacek, S. Cholia, D. Gunter, D. Skinner, G. Ceder, K.A. Persson, Commentary: the materials project: a materials genome approach to accelerating materials innovation, Apl. Mater. 1 (2013), <https://doi.org/10.1063/1.4812323>.
- [51] J.E. Saal, S. Kirklin, M. Aykol, B. Meredig, C. Wolverton, Materials design and discovery with high-throughput density functional theory: the open quantum materials database (OQMD), JOM (J. Occup. Med.) 65 (2013) 1501–1509, <https://doi.org/10.1007/s11837-013-0755-4>.
- [52] K. Choudhary, K.F. Garrity, A.C.E. Reid, B. DeCost, A.J. Biacchi, A.R. Hight Walker, Z. Trautt, J. Hattrick-Simpers, A.G. Kusne, A. Centrone, A. Davydov, J. Jiang, R. Pachter, G. Cheon, E. Reed, A. Agrawal, X. Qian, V. Sharma, H. Zhuang, S. V. Kalinin, B.G. Sumpter, G. Pilania, P. Acar, S. Mandal, K. Haule, D. Vanderbilt, K. Rabe, F. Tavazza, The joint automated repository for various integrated simulations (JARVIS) for data-driven materials design, Npj Comput. Mater. 6 (2020), <https://doi.org/10.1038/s41524-020-00440-1>.
- [53] A. Klaveness, O. Swang, H. Fjellvåg, Formation enthalpies of NaMgH_3 and KMgH_3 : a computational study, Europhys. Lett. 76 (2006) 285–290, <https://doi.org/10.1209/epl/i2006-10261-y>.
- [54] H. Zhang, S. Shang, J.E. Saal, A. Saengdeejing, Y. Wang, L.Q. Chen, Z.K. Liu, Enthalpies of formation of magnesium compounds from first-principles calculations, Intermetallics 17 (2009) 878–885, <https://doi.org/10.1016/j.intermet.2009.03.017>.
- [55] T. Le Bahers, M. Rérat, P. Sautet, Semiconductors used in photovoltaic and photocatalytic devices: assessing fundamental properties from DFT, J. Phys. Chem. C 118 (2014) 5997–6008, <https://doi.org/10.1021/jp409724c>.
- [56] B. Huang, J.N. Hart, DFT study of various tungstates for photocatalytic water splitting, Phys. Chem. Chem. Phys. 22 (2020) 1727–1737, <https://doi.org/10.1039/c9cp05944j>.
- [57] P. Meti, H.H. Park, Y.D. Gong, Recent developments in pyrazine functionalized π -conjugated materials for optoelectronic applications, J. Mater. Chem. C. 8 (2020) 352–379, <https://doi.org/10.1039/c9tc05014k>.

- [58] K. Thakar, S. Lodha, Optoelectronic and photonic devices based on transition metal dichalcogenides, *Mater. Res. Express* 7 (2019), <https://doi.org/10.1088/2053-1591/ab5c9c>.
- [59] M.R. Ashwin Kishore, A.O. Sjøstad, P. Ravindran, Influence of hydrogen and halogen adsorption on the photocatalytic water splitting activity of C2N monolayer: a first-principles study, *Carbon* N. Y. 141 (2019) 50–58, <https://doi.org/10.1016/j.carbon.2018.08.072>.
- [60] M.R. Ashwin Kishore, P. Ravindran, Tailoring the electronic band gap and band edge positions in the C2N monolayer by P and as substitution for photocatalytic water splitting, *J. Phys. Chem. C* 121 (2017) 22216–22224, <https://doi.org/10.1021/acs.jpcc.7b07776>.
- [61] K. Momma, F. Izumi, VESTA 3 for three-dimensional visualization of crystal, volumetric and morphology data, *J. Appl. Crystallogr.* 44 (2011) 1272–1276, <https://doi.org/10.1107/S0021889811038970>.
- [62] J.A. Abraham, G. Pagare, S.P. Sanyal, Electronic structure, electronic charge density, and optical properties analysis of GdX 3 (X = In, Sn, Tl, and Pb) compounds: DFT calculations, *Ind. J. Mater. Sci.* 2015 (2015) 1–11, <https://doi.org/10.1155/2015/296095>.
- [63] A. Natic, Y. Abid, R. Moubah, F. Khelifaoui, E.K. Hlil, H. Zaari, A. Benyoussef, M. Abid, H. Lassri, Structural, elastic, electronic and optical properties of RbPbI3 perovskites studied using ab-initio calculations, *Phase Transitions* 93 (2020) 54–61, <https://doi.org/10.1080/01411594.2019.1699087>.
- [64] N. Prudhvi Raju, R. Thangavel, Theoretical investigation of spin-orbit coupling on structural, electronic and optical properties for CuAB2 (A = Sb, Bi; B = S, Se) compounds using Tran-Blaha-modified Becke-Johnson method: a first-principles approach, *J. Alloys Compd.* 2 (2020), 154621, <https://doi.org/10.1016/j.jallcom.2020.154621>.
- [65] P.D. Sreedevi, R. Vidya, P. Ravindran, Earth-abundant nontoxic direct band gap semiconductors for photovoltaic applications by ab-initio simulations, *J. Sol. Energy.* 190 (2019) 350–360, <https://doi.org/10.1016/j.solener.2019.08.011>.
- [66] L.M. Yang, P. Vajeeston, P. Ravindran, H. Fjellvåg, M. Tilset, Theoretical investigations on the chemical bonding, electronic structure, and optical properties of the metal-organic framework MOF-5, *Inorg. Chem.* 49 (2010) 10283–10290, <https://doi.org/10.1021/ic100694w>.
- [67] F. Wooten, *Optical Properties of Solids*, Academic Press, 2013.
- [68] M. Fox, G.F. Bertsch, Optical properties of solids, *Am. J. Phys.* 70 (2002) 1269–1270, <https://doi.org/10.1119/1.1691372>.
- [69] A.C. Ulpe, T. Bredow, GW-BSE calculations of electronic band gap and optical spectrum of ZnFe2O4: effect of cation distribution and spin configuration, *ChemPhysChem* 21 (2020) 546–551, <https://doi.org/10.1002/cphc.201901088>.
- [70] T. Ouahrani, A.H. Reshak, R. Khenata, B. Amrani, M. Mebrouki, A. Otero-de-la-Roza, V. Luaña, Ab-initio study of the structural, linear and nonlinear optical properties of CdAl2Se4 defect-chalcopyrite, *J. Solid State Chem.* 183 (2010) 46–51, <https://doi.org/10.1016/j.jssc.2009.09.034>.
- [71] J. Liu, B. Cheng, New understanding of photocatalytic properties of zigzag and armchair g-C3N4 nanotubes from electronic structures and carrier effective mass, *Appl. Surf. Sci.* 430 (2018) 348–354, <https://doi.org/10.1016/j.apsusc.2017.06.205>.
- [72] N.M. Rahman, M. Adnaan, D. Adhikary, M. Islam, M.K. Alam, First-principles calculation of the optoelectronic properties of doped methylammonium lead halide perovskites: a DFT-based study, *Comput. Mater. Sci.* 150 (2018) 439–447, <https://doi.org/10.1016/j.commatsci.2018.04.048>.
- [73] Y.S. Kim, M. Marsman, G. Kresse, F. Tran, P. Blaha, Towards efficient band structure and effective mass calculations for III-V direct band-gap semiconductors, *Phys. Rev. B Condens. Matter* 82 (2010) 1–11, <https://doi.org/10.1103/PhysRevB.82.205212>.
- [74] R.B. Araujo, J.S. De Almeida, A. Ferreira Da Silva, Electronic properties of III-nitride semiconductors: a first-principles investigation using the Tran-Blaha modified Becke-Johnson potential, *J. Appl. Phys.* 114 (2013), <https://doi.org/10.1063/1.4829674>.
- [75] A.V. Rodina, M. Dietrich, A. Göldner, L. Eckey, A. Hoffmann, A.L. Efros, M. Rosen, B.K. Meyer, Free excitons in wurtzite GaN, *Phys. Rev. B Condens. Matter* 64 (2001) 1152041–11520419, <https://doi.org/10.1103/physrevb.64.115204>.
- [76] L.K. Gao, Y.L. Tang, Theoretical study on the carrier mobility and optical properties of CsPbI3 by DFT, *ACS Omega* 6 (2021) 11545–11555, <https://doi.org/10.1021/acsomega.1c00734>.
- [77] X. Ma, Z. Li, J. Yang, Efficient direct band gap photovoltaic material predicted via doping double perovskites Cs2AgBiX6 (X = Cl, Br), *J. Phys. Chem. C* 125 (2021) 10868–10875, <https://doi.org/10.1021/acs.jpcc.1c01871>.